

Design and Analysis of 3D Capacitive Accelerometer for Automotive Applications

Alessandro Porta

Dipartimento di Ingegneria dell'Informazione

Università di Pisa

Pisa, Italy

a.porta2@studenti.unipi.it

Abstract—This work presents the design and analysis of a 3D accelerometer for automotive applications, based on a study originally presented at the 2011 COMSOL Conference in Bangalore. The primary objective of this analysis is to verify the accuracy of the results reported in the original work. The performance evaluation of the device is conducted using COMSOL Multiphysics 6.0, focusing on key parameters such as the equivalent elastic constant of the springs, maximum displacement, and maximum stress under horizontal and vertical loads. Furthermore, for a fixed acceleration value (100g), the dependence of the displacement on the angle between the x-axis and y-axis is analyzed.

I. INTRODUCTION

The use of airbags has become a necessity in today's world to enhance safety during collisions. Various devices, such as accelerometers, gyroscopes, and others, are essential for detecting collisions. When the signal in the sensing device reaches a threshold value, the airbag must deploy within a few milliseconds. Therefore, rapid detection and high sensitivity of the sensing device are critical requirements.

In the study we refer to [1], the focus is on MEMS accelerometers that utilize changes in capacitance caused by negative acceleration. Additionally, accelerometers based on piezoresistive principles, such as those discussed in [1], are also common. However, the use of comb-drive MEMS accelerometers is preferred due to the following advantages:

- **Noise and temperature:** Capacitive accelerometers are ideal enough since they are less prone to noise and temperature as compared to piezoresistive accelerometers.
- **Power consumption:** Capacitive accelerometers have low power consumption.
- **Scale factor stability:** excellent bias and scale factor stability.
- **Sensitivity:** They have excellent sensitivity.
- **Base material:** Capacitive sensing is independent of the base material and relies on the variation of capacitance when the geometry of the capacitor is changing.

II. ARCHITECTURE DESIGN

The proposed accelerometer is designed to sense acceleration in the range of $\pm 100g$ while also being capable of withstanding a maximum shock of additional g-forces. In the referenced study, the device is specified to endure up to $\pm 150g$; however, in this work, we have achieved a capability of $\pm 200g$.

This improvement is attributed to the rigid structure of the accelerometer, which enables it to withstand higher g-forces.

A. Mechanical Equivalent

The mechanical structure of an accelerometer can be modeled as a second-order mass-spring-damper system. At the core of this system is a spring-supported proof mass, often paired with dampers to provide the necessary damping effect. These springs and dampers are connected to an external shell. When acceleration is applied, the proof mass undergoes a displacement, $x(t)$, relative to the shell.

In the case of an inertial accelerometer, a mechanical sensing element translates the applied acceleration into a force. This force results in a displacement, which, in turn, causes a change in capacitance. The change in capacitance is detected and converted into an equivalent electrical signal.

The proof mass resists motion due to its inertia when subjected to external forces acting on the reference frame. It is connected to the frame via springs and experiences damping effects from the surrounding gas or internal dissipation within the springs. These dynamics form the basis of the accelerometer's mechanical behavior.

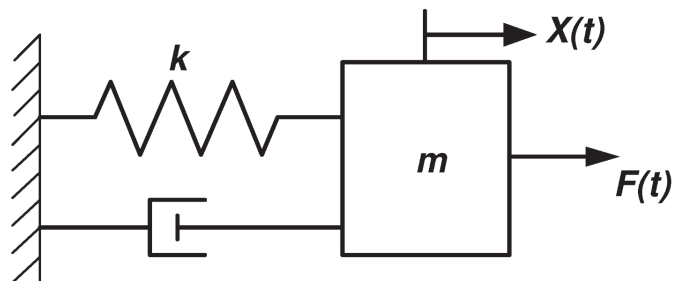


Fig. 1: Mass-spring-damper system.

However, the structure presented in this work differs from a simple one-axis, single-spring, second-order system. As shown in Fig. 2, the accelerometer is designed to handle loads in multiple directions—specifically along the x and y axes. For each direction of the load, a distinct mechanical equivalent is required to describe the system's behavior accurately.

The key task is to determine the equivalent elastic constant for each type of load. This involves analyzing the spring

configuration and its response to loads applied along the x or y axis. The equivalent elastic constants are critical for understanding the mechanics of the structure under different loading conditions.

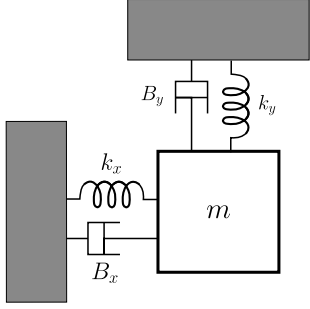


Fig. 2: Double axis mass-spring-damper system

B. Structural design

The proposed novel accelerometer, as illustrated in Fig. 3, consists primarily of central movable fingers attached to the proof mass and multiple fixed fingers. These fixed electrode plates are anchored to a glass substrate. The sensing capacitance is generated between the movable and fixed fingers, which are aligned parallel to each other. The sensing mechanism features a bilateral comb design, with the sensing direction in lateral comb-finger microaccelerometers lying within the plane of the proof mass (x-y directions).

In the absence of acceleration, the central proof mass remains in equilibrium, and the capacitance is C_0 . When acceleration is applied, the movable fingers are displaced due to the inertial force acting on the proof mass. This displacement changes the spacing between the movable fingers and the fixed plates, leading to a variation in the total measured capacitance.

The movable and fixed fingers form a parallel plate capacitor, and the capacitance can be estimated using Equation 1:

$$C = \frac{\epsilon A}{d} \quad (1)$$

Here, ϵ is the permittivity, A represents the total overlap area of all the fingers in the sensing region, and d is the separation between adjacent fingers. Since the capacitance of a single finger is relatively low, achieving a higher signal requires increasing either the overlap area or the number of fingers.

C. Structural sizing

Springs: As the accelerometer functions as a second-order damper system, the springs play a critical role in its operation. These springs are anchored at fixed points, and the force exerted on them results in the displacement of the proof mass. As shown in Fig. 3, there are four springs: two along the x-axis and two along the y-axis, arranged symmetrically, with each pair being identical. Each spring has a stiffness tensor that describes its mechanical response in all directions. However, as we focus on loads applied along the x and y axes, we are primarily interested in the stiffness components along these axes. Notably,

the stiffness tensor includes off-diagonal elements that capture coupling effects between x and y directions under specific load conditions.

The springs are categorized as x-springs (Fig. 4a) and y-springs (Fig. 4b), depending on whether their primary alignment is along the x-axis or the y-axis.

As shown in Fig. 5, each spring is composed of two distinct parts: a double U-shaped spring and a crab-leg structure. The dominant component varies depending on the direction of the load—either along the spring's axis or perpendicular to it.

Table I shows the x-spring and y-spring dimensions, according to Fig. 5.

Parameter [nm]	x-spring	y-spring
L_1	1000	1000
w_1	10	20
L_2	500	150
w_2	50	20

TABLE I: Dimensions of x-spring and y-spring

The stiffness along the x-axis (y-axis) for the x-spring (y-spring), denoted as k_{xx} (k_{yy}), can be calculated using the equation provided in [2] based on the work done in [3]:

$$k_{xx} = Eh \left(\frac{w_1}{L_1/2} \right)^3 \quad (2)$$

Conversely, the stiffness along the y-axis (x-axis) for the x-spring (y-spring), denoted as k_{xy} (k_{yx}), can be calculated using the equation also provided in [2] based on the work done in [3]:

$$k_{xy} = \frac{Eh \left(\frac{w_2/2}{L_2} \right)^3 \left(L_2 - \frac{L_1/2}{3.6} \right)}{L_1/2 + 0.3L_2} \quad (3)$$

In both equations, $E = 131$ GPa (Young's modulus), as given in [1], and $h = 40$ nm represents the height of the entire structure.

According to Eq. 2, the calculated stiffness values are:

$$k_{xx_{analytic}} = 0.042 \text{ N/m}, \quad k_{yy_{analytic}} = 0.671 \text{ N/m}.$$

Similarly, according to Eq. 3, the calculated stiffness values are:

$$k_{xy_{analytic}} = 0.938 \text{ N/m}, \quad k_{yx_{analytic}} = 1.797 \text{ N/m}.$$

The total stiffness along each axis, considering the contributions of all four springs, is given as:

$$k_{x_{analytic}} = 2k_{xx_{analytic}} + 2k_{yx_{analytic}} = 3.677 \text{ N/m}$$

$$k_{y_{analytic}} = 2k_{yy_{analytic}} + 2k_{xy_{analytic}} = 3.217 \text{ N/m}$$

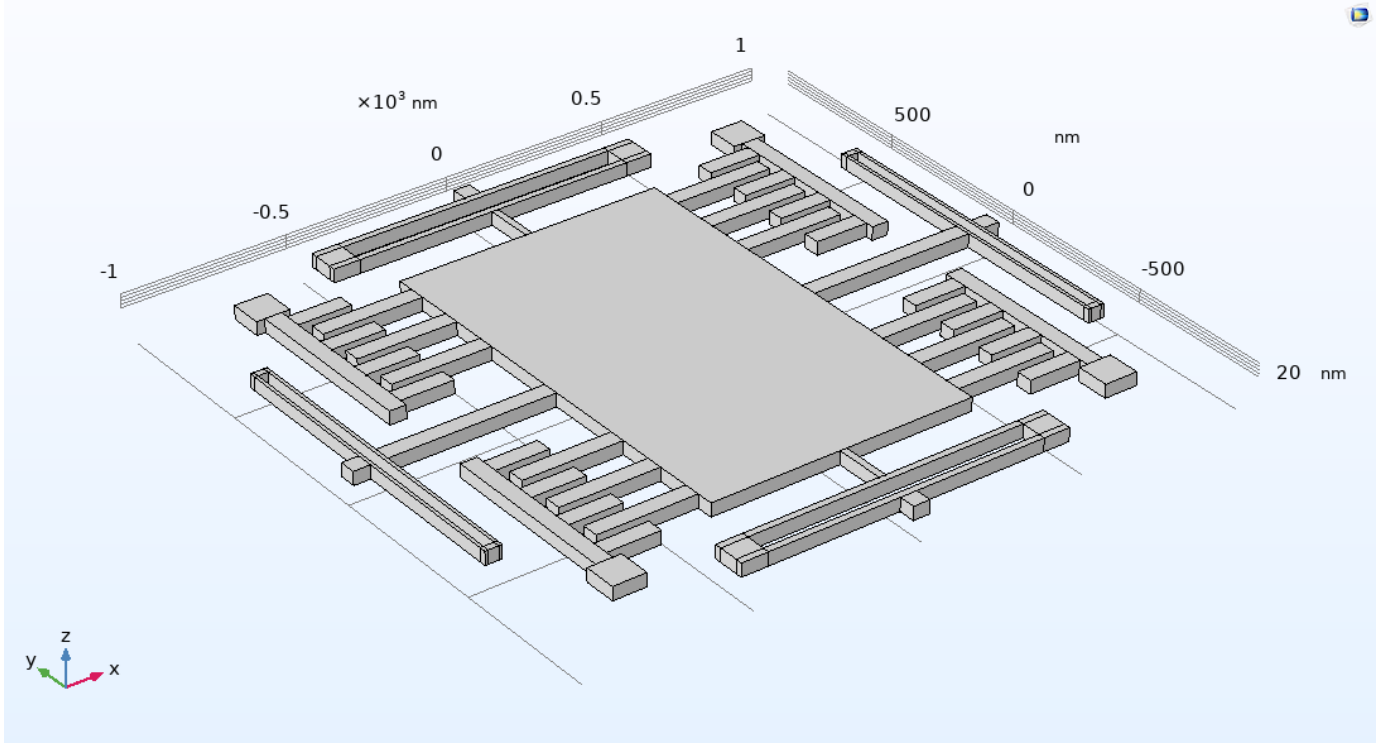
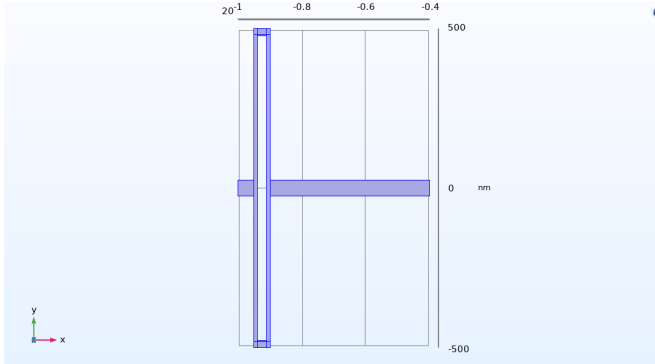
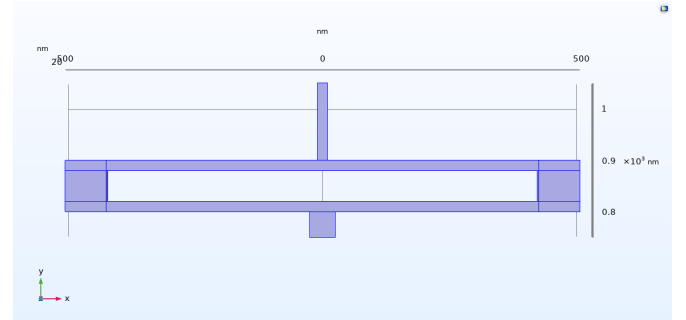


Fig. 3: 3D capacitive accelerometer



(a) x-spring



(b) y-spring

Fig. 4: Comparison of the x-spring and y-spring structures: (a) x-spring, (b) y-spring.

Proof Mass and Fingers: In [1], the following mass values are reported:

- Mass of the central proof mass: 9.69×10^{-17} kg
- Mass of fixed and movable fingers: 2.8705×10^{-17} kg
- Total mass: 12.5605×10^{-17} kg

Considering $h = 40$ nm and extrapolating the aspect ratios from the figures provided in the paper, the following dimensions were determined:

- proof mass: $1300 \text{ nm} \times 800 \text{ nm} \times 40 \text{ nm}$
- single movable finger: $300 \text{ nm} \times 50 \text{ nm} \times 40 \text{ nm}$
- single fixed finger: $160 \text{ nm} \times 50 \text{ nm} \times 40 \text{ nm}$

Static Capacitances: Table II presents the dimensions of the T-shaped capacitances, as illustrated in Fig. 6.

Parameter	Dimensions [nm]
w	50
d_l	25
d_{t1}	25
d_{t2}	165
t	135

TABLE II: T-shaped capacitance dimensions.

As shown in Fig. 3, there are a total of 12 T-shaped capacitances. Each capacitance consists of two transverse capacitances and two longitudinal capacitances. For each T-shape, the static capacitances (without any load) can be

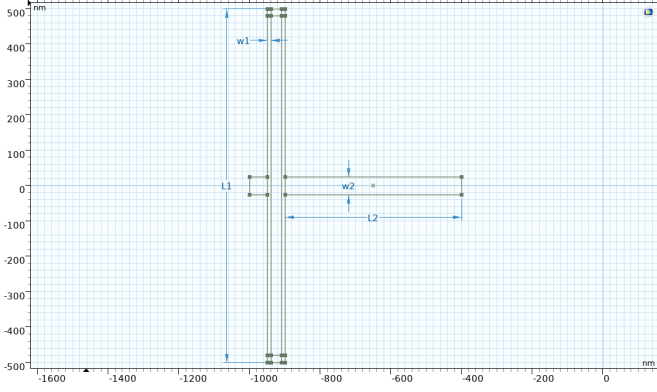


Fig. 5: spring dimensions

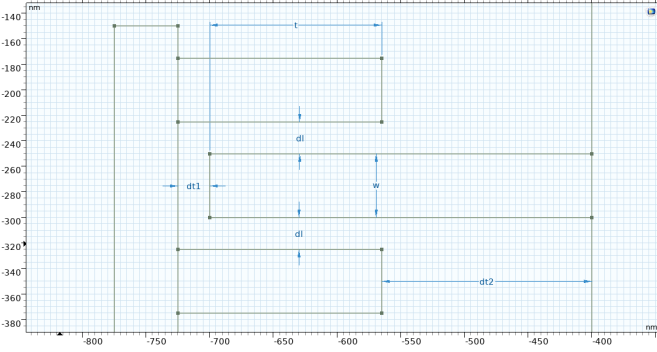


Fig. 6: T-shaped capacitance

estimated using Equation 4 (for transverse capacitances) and Equation 5 (for longitudinal capacitances).

$$C_l = \varepsilon \frac{ht}{d_l} \quad (4)$$

$$C_t = \varepsilon \frac{hw}{d_t} \quad (5)$$

Using Eq. 4 and Eq. 5, the calculated values are:

$$C_l = 1.912504568860800 \times 10^{-18} \text{ F}$$

$$C_{t_1} = 7.08335025504 \times 10^{-19} \text{ F}$$

$$C_{t_2} = 1.0732348871272725 \times 10^{-19} \text{ F}$$

The total capacitance for a single T-shaped:

$$C_{static} = 2C_l + C_{t_1} + C_{t_2} = 4.640667651938327 \times 10^{-18} \text{ F}$$

Finally, the total capacitance, considering 12 T-shaped:

$$C_{static_{tot}} = 12 \times C_{tot} = 5.568801182325993 \times 10^{-17} \text{ F}$$

These calculations were performed using a Python script with a precision of 50 decimal places to accurately capture and appreciate the variations in capacitance.

1) *Capacitances with load applied:* When a load is applied, the displacement resulting from the application of the load causes a variation in capacitances. As shown in [1], the displacement in both the y - and x -direction loads are on the order of femtometers (fm). For the calculations that follow, we consider the displacement under y -load for the case of 100g, which we obtained from our simulation ($v = 46.06 \text{ fm}$), as will be discussed in Section IV. We have chosen to make analytical calculations under y -load for simplicity, because in this section we are primarily interested in determining the order of magnitude of the percentage variation. This will allow us to compare the analytical approach with the results obtained from simulations.

Under a y -load, the variation in capacitance is limited to C_l :

$$C_{l_{var}} = \varepsilon \frac{ht}{d_l - v} \quad (6)$$

$$C_{l_{2var}} = \varepsilon \frac{ht}{d_l + v} \quad (7)$$

In contrast, for C_{t_1} and C_{t_2} , there is no theoretical variation under this condition.

Using Eq. 6 and Eq. 7, the calculated values are:

$$C_{l_{var}} = 1.912508112355831 \times 10^{-18} \text{ F}$$

$$C_{l_{2var}} = 1.9125010253789006 \times 10^{-18} \text{ F}$$

The total capacitance for a single T-shaped:

$$C_{var} = C_{l_{var}} + C_{l_{2var}} + C_{t_1} + C_{t_2} = 4.640667651951459 \times 10^{-18} \text{ F}$$

Finally, the total capacitance, considering 12 T-shaped:

$$C_{var_{tot}} = 12 \times C_{tot} = 5.568801182341751 \times 10^{-17} \text{ F}$$

So, using what was found in II-C,

$$C_{delta} = C_{var_{tot}} - C_{static_{tot}} = 1.575749658178971 \times 10^{-28} \text{ F}$$

$$C_{delta_{perc}} = 100 \times \frac{C_{var_{tot}} - C_{static_{tot}}}{C_{static_{tot}}} = 2.829603008956422 \times 10^{-10} \%$$

III. USE OF COMSOL MULTIPHYSICS

The designed accelerometer was simulated using COMSOL Multiphysics 6.0.

The objective of this work is to replicate the structure and simulations performed in [1] to verify the accuracy of the results reported in the reference study. Furthermore, this work focuses on evaluating the following key aspects:

- 1) Determining the equivalent elastic constant of the springs for both horizontal and vertical loads, and comparing the obtained values with the theoretical results provided in [1].
- 2) Assessing the maximum deflection, maximum stress, and capacitance of the structure as functions of vertical and

horizontal accelerations. The analysis includes at least 10 different acceleration values to ensure the structure's correct performance.

- 3) For a specific acceleration value, evaluating the dependency of deflection on the direction of the applied acceleration. This involves analyzing at least 10 different angles between the y-axis and the x-axis.

For a more complete analysis, the stiffness of the x and y springs will be simulated individually in Section V. This will enable a detailed comparison between the stiffness values obtained from the full-structure simulation (Section IV), the single-spring simulations (Section V), and the theoretical values discussed in Section II.

A. Model Definition

To simulate the entire structure, the simulations were conducted using the Electromechanics Multiphysics module, which combines the Mechanical and Electrostatic modules. The simulations were performed as a stationary study.

The simulation results will help validate the original study and provide additional insights into the mechanical and electrical performance of the accelerometer under varying conditions.

B. General Parameters and Materials

The entire structure is made of polysilicon, with a Young's modulus $E = 131 \text{ GPa}$ and a density $\rho = 2330 \text{ kg/m}^3$. The surrounding box enclosing the accelerometer is filled with air.

C. Electrostatics

Despite the referenced work using a potential difference of 1 V between the movable and fixed parts, this work prefers to use 1 mV. This choice reduces the influence of the electrostatics module on the solid mechanics module, as the higher voltage causes a static displacement (without any applied load) significantly greater than that in the case study.

In this simulation, the fixed fingers are set to ground potential, while a potential of 1 mV is applied to the movable parts (Terminal).

D. Solid Mechanics

In this module, boundary fixed constraints are applied to the anchor and the fixed fingers. The entire structure is subjected to a body load, which can act along the x-axis, the y-axis, or at an angle between them.

The load is expressed in terms of force per unit volume. By utilizing parameter definitions, it is possible to perform various case studies with different acceleration values (expressed in terms of g's as the load).

E. Multiphysics

As mentioned earlier, the study was performed using the Electromechanics module, which enables coupling between the solid mechanics and electrostatics modules. This coupling allows the observation of variations in capacitance caused by structural displacements.

F. Mesh

For the mesh, a physics-controlled mesh with a normal element size was used. This choice ensures that the results obtained are consistent with analytical studies and, in some cases, with the referenced text.

IV. STUDY AND RESULTS

Three types of studies were performed: y-load, x-load, and alpha-load (where alpha represents the angle between the x-axis and the y-axis). For each study, an auxiliary sweep was conducted for the acceleration, ranging from 0 g to 200 g with steps of 20 g. This approach allows testing of the structure under normal operating conditions (below 100 g) and stressed conditions (up to 200 g).

A. Y Load

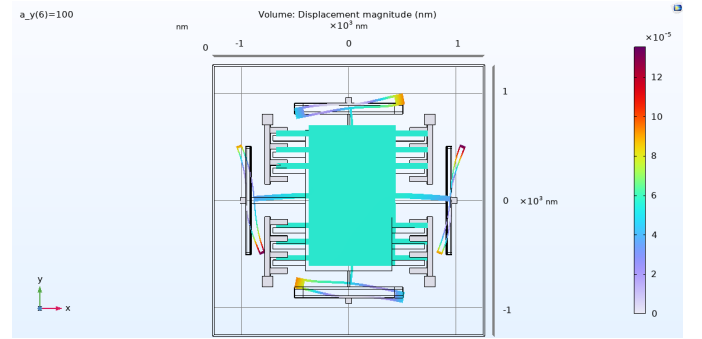


Fig. 7: Displacement under 100g

1) *Displacement*: Firstly, as shown in Fig. 7, the displacement under 100 g in the y-direction is illustrated.

Subsequently, the maximum displacement in the y-direction is calculated using a global definition, $\text{maxop1}(v)$, where $\text{maxop1}()$ is a function used to determine the maximum value of a quantity across the proof mass and fixed fingers.

Table III presents the values of maximum displacement for different acceleration levels (g).

a_y (g)	Max Displacement (nm)
0	1.220×10^{-7}
20	9.292×10^{-6}
40	1.847×10^{-5}
60	2.767×10^{-5}
80	3.686×10^{-5}
100	4.606×10^{-5}
120	5.526×10^{-5}
140	6.446×10^{-5}
160	7.366×10^{-5}
180	8.286×10^{-5}
200	9.205×10^{-5}

TABLE III: Maximum displacement under y-load for various acceleration levels.

As can be seen, the maximum displacement under 100 g is 46.06 fm, while in the referenced work it is 600 fm.

The discrepancy arises because the referenced work lacks key information about the model definition and sizing. It is likely that the structure in this work is more rigid than the one described in the referenced work.

2) *Stiffness*: The equivalent elastic constant under a y-load is calculated using the expression:

$$k_y = \frac{\text{intop1}(F_{y\text{density}})}{\text{maxop1}(v)},$$

where $\text{intop1}()$ is a function defined to integrate over the proof mass and movable fingers to determine the total force, and $\text{maxop1}()$ is a function used to calculate the maximum displacement of the proof mass and movable fingers.

The value obtained (under 100g) is

$$k_{y\text{simul,entire}} = 2.421 \text{ N/m}$$

which remains almost constant over the tested range of accelerations.

It is important to compare this result with the analytical value derived in Section II, where $k_{y\text{analytic}} = 3.217 \text{ N/m}$. The value obtained from the simulation is consistent with the analytical result, suggesting that it is reasonable to consider the simulation result accurate.

In contrast, the referenced work [1] reports a stiffness of 13.5829 N/m. However, [1] does not provide specific formulas for the stiffness components k_{xy} and k_{yx} , making it more appropriate to compare the simulation result with the analytical value obtained in this work.

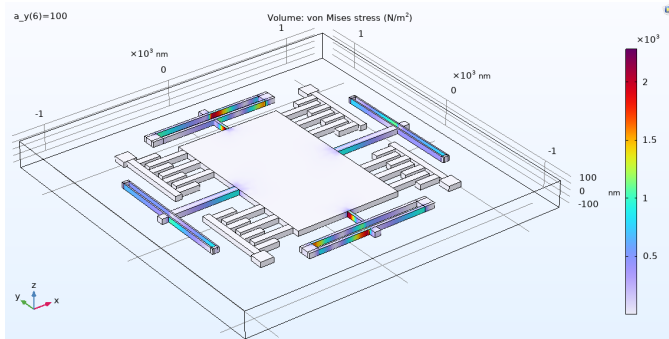


Fig. 8: Stress under 100g

3) *Stress*: Firstly, as shown in Fig. 8, the stress under 100 g in the y-direction is illustrated.

Subsequently, the maximum stress is calculated using a global definition, $\text{maxop1}(\text{solid.mises})$, where $\text{maxop1}()$ is a function used to determine the maximum value of a quantity across the entire structure.

Table IV presents the values of maximum displacement for different acceleration levels (g).

Comparing the maximum stress under 100 g with the value provided in [1] (in the order of 10^{11} N/m^2), there is a significant difference. This discrepancy is likely due to the different sizing of the structures.

a_y (g)	Max Stress (N/m ²)
0	1218.63
20	1218.87
40	1219.13
60	1219.39
80	1219.66
100	1219.94
120	1220.22
140	1220.51
160	1220.82
180	1221.13
200	1221.44

TABLE IV: Maximum stress under y-load for various acceleration levels.

a_y (g)	Y-Load Capacitance (F)
0	$1.5653953632810892 \times 10^{-16}$
20	$1.5653953632810907 \times 10^{-16}$
40	$1.5653953641256130 \times 10^{-16}$
60	$1.5653953649703286 \times 10^{-16}$
80	$1.5653953658152314 \times 10^{-16}$
100	$1.5653953666603140 \times 10^{-16}$
120	$1.5653953675055986 \times 10^{-16}$
140	$1.5653953683510648 \times 10^{-16}$
160	$1.5653953691967120 \times 10^{-16}$
180	$1.5653953700425743 \times 10^{-16}$
200	$1.5653953708886082 \times 10^{-16}$

TABLE V: Capacitance under y-load for various acceleration levels.

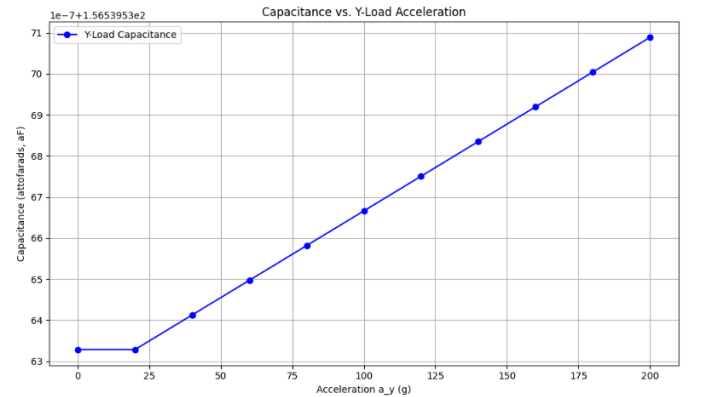


Fig. 9: Capacitance variation for y load

4) *Capacitance*: Table V reports the variation of capacitance under different acceleration levels. Firstly, it is evident that the simulation results align with the analytical calculations performed in Section II.

The total capacitance obtained analytically is $C_{\text{tot}} =$

5.569×10^{-17} F, while the simulated total capacitance without load (as seen in the first line of Table V) is approximately $C_{tot_{simul}} = 1.565 \times 10^{-16}$ F. The slight discrepancy can be attributed to edge effects, which are not considered in the analytical calculation. These effects contribute to the additional capacitance observed in the simulation.

Furthermore, it is possible to observe the minimal variation in capacitance values under load, as we expected.

Indeed, considering a 100g load:

$$C_{delta_{simul}} = c_{100} - c_0 = 3.3792247242487493 \times 10^{-25}$$

$$C_{delta_{perc_{simul}}} = 2.1587036754509415 \times 10^{-7}\%$$

This minimal variation is consistent with the changes calculated analytically in Section II-C1.

B. X Load

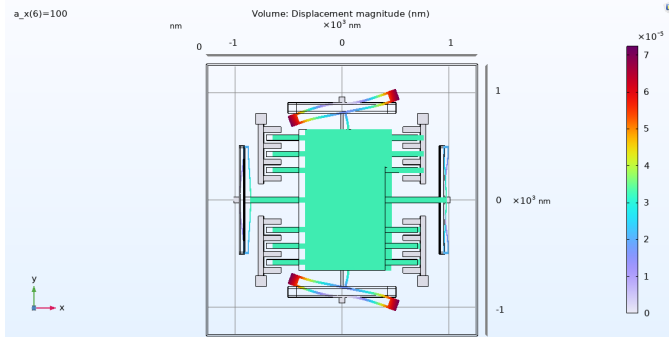


Fig. 10: Displacement under 100g

1) *Displacement*: For the x-load case, Fig. 10 depicts the displacement in the x-direction under an acceleration of 100 g.

The maximum displacement in the x-direction is then evaluated using a global definition, $\text{maxop1}(u)$, where $\text{maxop1}()$ computes the maximum value as for Y-Load.

Table VI provides the maximum displacement values obtained for various acceleration levels (g).

As can be seen, the maximum displacement under 100 g is 32.43 fm, while in the referenced work it is 12 fm.

2) *Stiffness*: For the x-load case, the equivalent elastic constant is calculated similarly to the y-load, using the expression:

$$k_x = \frac{\text{intop1}(F_{x_{density}})}{\text{maxop1}(u)},$$

where $\text{intop1}()$ and $\text{maxop1}()$ refers to the same operators as for Y Load.

The value obtained (under 100g) is

$$k_{x_{simul,entire}} = 3.438 \text{ N/m},$$

which, like k_y , remains almost constant over the tested range of accelerations.

Compared to the analytical value derived in Section II, $k_{x_{analytic}} = 3.677 \text{ N/m}$, the simulated result shows good

a_x (g)	Max Displacement (nm)
0	4.477×10^{-10}
20	6.486×10^{-6}
40	1.297×10^{-5}
60	1.946×10^{-5}
80	2.594×10^{-5}
100	3.243×10^{-5}
120	3.892×10^{-5}
140	4.540×10^{-5}
160	5.189×10^{-5}
180	5.837×10^{-5}
200	6.486×10^{-5}

TABLE VI: Maximum displacement under x-load for various acceleration levels.

agreement. This suggests that the simulation result is reasonable and accurate.

As with the y-load case, the referenced work [1] reports a significantly higher stiffness value of 54.3364 N/m. However, due to the lack of specific formulas for the stiffness components k_{xy} and k_{yx} in [1], the comparison with the analytical results obtained in this work remains the most reliable benchmark.

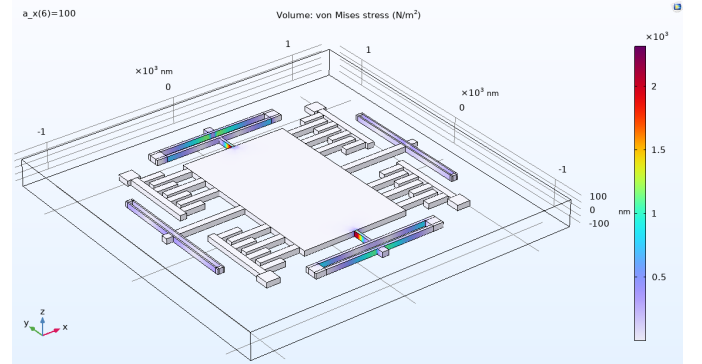


Fig. 11: Stress under 100g in the x-direction.

3) *Stress*: As shown in Fig. 11, the stress under 100 g in the x-direction is depicted.

The maximum stress is calculated using a global definition, $\text{maxop1}(\text{solid.mises})$, where $\text{maxop1}()$ computes the maximum value of a quantity across the entire structure.

Table VII lists the maximum stress values for different acceleration levels (a_x).

Comparing the maximum stress under 100 g with the value provided in [1] (in the order of 10^{11} N/m^2), there is again a significant difference. This discrepancy is likely due to the different sizing and design parameters of the structures.

4) *Capacitance*: Table VIII reports the capacitance values under x-load for various acceleration levels. As observed, the capacitance variation is compatible with femtometer displacement, as discussed previously.

a_x (g)	Max Stress (N/m ²)
0	0.351
20	243.754
40	487.472
60	731.190
80	974.909
100	1218.627
120	1462.345
140	1706.064
160	1949.782
180	2193.500
200	2437.218

TABLE VII: Maximum stress under x-load for various acceleration levels.

a_x (g)	X-Load Capacitance (F)
0	$1.5653953643116492 \times 10^{-16}$
20	$1.5653953643116628 \times 10^{-16}$
40	$1.5653953641055118 \times 10^{-16}$
60	$1.565395363899372 \times 10^{-16}$
80	$1.5653953636932466 \times 10^{-16}$
100	$1.5653953634871557 \times 10^{-16}$
120	$1.5653953632810838 \times 10^{-16}$
140	$1.5653953630750378 \times 10^{-16}$
160	$1.565395362869004 \times 10^{-16}$
180	$1.5653953626630118 \times 10^{-16}$
200	$1.5653953624570217 \times 10^{-16}$

TABLE VIII: Capacitance under x-load for various acceleration levels.

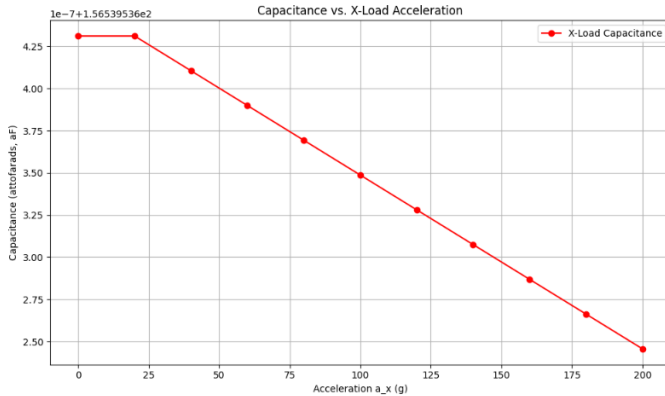


Fig. 12: Capacitance variation for x load

C. Alpha Load

As a final simulation, the dependence of deflection on the direction of the applied acceleration was analyzed for a total load of 100 g. To perform this simulation, the total acceleration was set as $a_{\text{tot}} = 100$, and the components a_x and a_y were

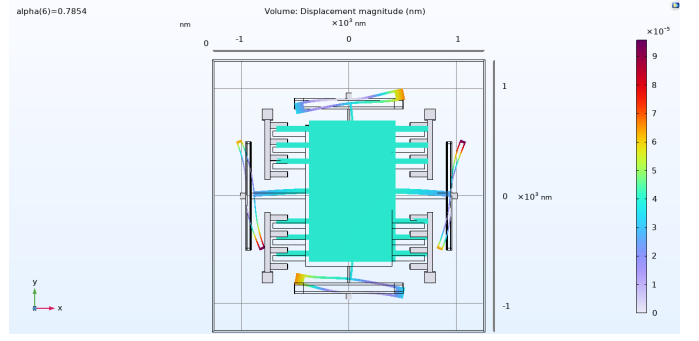


Fig. 13: Displacement under alpha Load

defined as:

$$a_x = a_{\text{tot}} \cdot \cos(\alpha), \quad a_y = a_{\text{tot}} \cdot \sin(\alpha),$$

where α is the angle relative to the x-axis.

Fig. ?? shows the displacement under a value of alpha load ($\pi/4$)

As in the previous simulations, the corresponding body loads were defined as:

$$F_{x_{\text{density}}} = a_x \cdot 2330 [\text{kg/m}^3] \cdot g_{\text{const}},$$

$$F_{y_{\text{density}}} = a_y \cdot 2330 [\text{kg/m}^3] \cdot g_{\text{const}}.$$

An auxiliary sweep was performed over α , ranging from 0 to $\pi/2$ with a step of $\pi/20$.

α (rad)	X Displacement (nm)	Y Displacement (nm)
0	3.243×10^{-5}	1.220×10^{-7}
$\frac{\pi}{20}$	3.205×10^{-5}	7.293×10^{-6}
$\frac{\pi}{10}$	3.088×10^{-5}	1.428×10^{-5}
$\frac{3\pi}{20}$	2.895×10^{-5}	2.094×10^{-5}
$\frac{\pi}{5}$	2.631×10^{-5}	2.709×10^{-5}
$\frac{\pi}{4}$	2.302×10^{-5}	3.257×10^{-5}
$\frac{3\pi}{10}$	1.917×10^{-5}	3.725×10^{-5}
$\frac{7\pi}{20}$	1.484×10^{-5}	4.101×10^{-5}
$\frac{2\pi}{5}$	1.015×10^{-5}	4.376×10^{-5}
$\frac{9\pi}{20}$	5.203×10^{-6}	4.544×10^{-5}
$\frac{\pi}{2}$	1.317×10^{-7}	4.599×10^{-5}

TABLE IX: Displacement vs. α for x and y directions.

Table IX shows the maximum displacement in the x and y directions for different angles, while Fig. 14 provides a plot of these values.

As observed, the first value corresponds to a 100 g x-load, as discussed in Section IV-B, while $\pi/2$ corresponds to a 100 g y-load, as described in Section IV-A. Furthermore, a decrease in the x-displacement is observed as the angle α increases. This aligns with the fact that the x-load is diminishing while the y-load is increasing, which is reflected in the increment of the y-displacement. It is important to note that the displacement is evaluated at both the proof mass and the movable fingers.

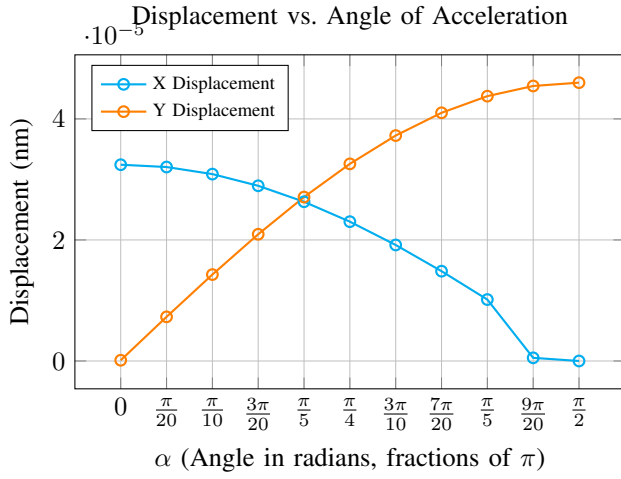


Fig. 14: Displacement vs. Angle of Acceleration: Comparison of X and Y Displacements.

V. SIMULATIONS OF SINGLE X-SPRING AND Y-SPRING

In this section, simulations of individual x-spring and y-spring are presented to determine the stiffness of each spring under x or y load. The goal is to establish a correspondence between the analytical results and the simulation outcomes of the entire structure.

A. Simulation Setup

For simplicity, this section focuses on the x-spring; however, the same considerations apply to the y-spring, with the roles of the x and y axes interchanged (i.e., x-load along the axis of the spring, and y-load perpendicular to the spring's axis).

The structure of each spring consists of two main components: the double U-shaped spring and the crab leg (or beam). Since the primary objective is to determine the stiffness, the simulation is set up as a solid mechanics study. The following boundary conditions are applied:

- 1) **X-Load:** A fixed constraint is applied to the anchor, and a boundary load is applied at the termination of the crab leg along the x-axis.
- 2) **Y-Load:** To simulate the presence of the proof mass, a guided termination (COMSOL: roller constraint) is applied to the end of the crab leg, and an edge load is applied along the y-axis.

It is important to note that, in these simulations, the mass of the springs is neglected as it is negligible compared to the proof mass. This approximation ensures that the results remain accurate and do not differ significantly from those obtained by including the spring mass.

As a body load, a total force compatible with the load of the entire structure was applied. Considering that each spring has its own stiffness (two in total for the four springs), a total force proportional to each analytically calculated stiffness was applied. This force is in the order of $F_{\text{tot}} = 10^{-14}$ N, ensuring the springs operate within their linear response range.

For a more accurate simulation, it would be interesting to perform a parametric analysis to determine the range of linearity for the springs. However, such an analysis is beyond the scope of this work.

Nevertheless, this approach ensures that the individual springs are subjected to the same conditions as they experience within the complete accelerometer structure.

B. Results

In figures 15, the displacement results for the four cases are shown: x-load and y-load for the x-spring, and x-load and y-load for the y-spring.

Subsequently, using global definitions, the four stiffness values (k) are calculated using the general expression:

$$k = \frac{F_{\text{tot}}}{\maxop1(u) \text{ (or } \maxop1(v))},$$

where the functions $\maxop1(u)$ and $\maxop1(v)$ retain the same meanings as described in previous sections.

The calculated stiffness values are as follows (with the first subscript indicating the type of spring, and the second subscript indicating the type of load):

$$\begin{aligned} k_{xx_{\text{simul,beam}}} &= 0.064 \text{ N/m}, \\ k_{xy_{\text{simul,beam}}} &= 0.944 \text{ N/m}, \\ k_{yy_{\text{simul,beam}}} &= 0.576 \text{ N/m}, \\ k_{yx_{\text{simul,beam}}} &= 1.874 \text{ N/m}. \end{aligned}$$

By summing the respective components, the total stiffness values are:

$$k_{x_{\text{simul,beam}}} = 3.876 \text{ N/m}, \quad k_{y_{\text{simul,beam}}} = 3.040 \text{ N/m}.$$

Table X presents the stiffness values obtained from the current simulations and the analytical results from Section II.

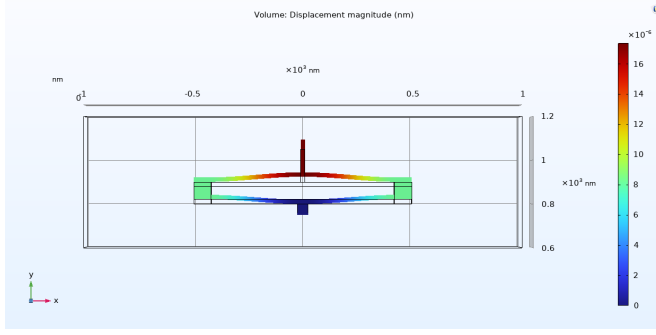
k [N/m]	Analytical	Simulated Beam
k_{yy}	0.671	0.576
k_{yx}	1.797	1.874
k_{xx}	0.042	0.064
k_{xy}	0.938	0.944

TABLE X: Stiffness of the single springs: analytical vs simulated

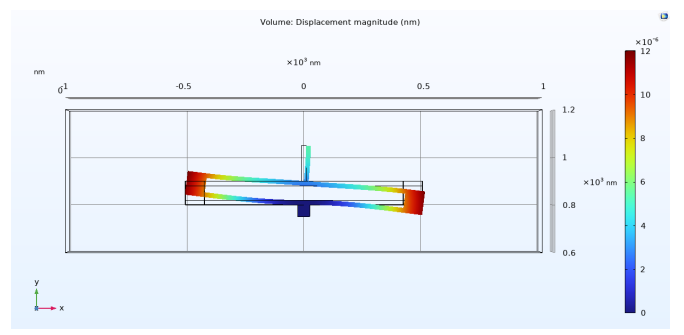
Finally, Table XI presents the total stiffness obtained in this simulation, in the analytical one and in the simulation of the entire structure.

k [N/m]	Analytical	Simulated entire	Simulated beam
k_y	3.217	2.421	3.040
k_x	3.677	3.438	3.876

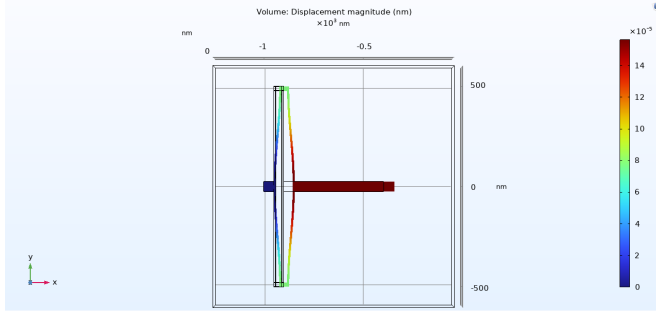
TABLE XI: Total stiffness: analytical vs simulated entire vs simulated beam



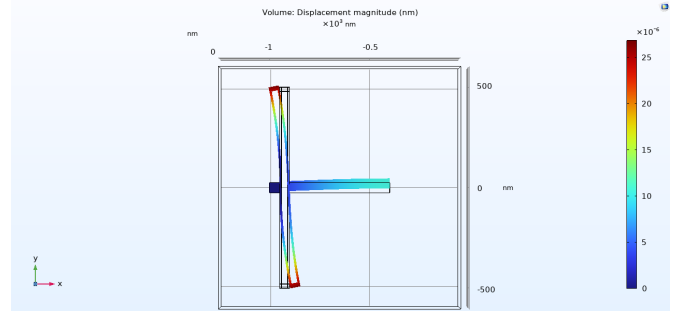
(a) v Displacement for y-spring (y load)



(b) u Displacement for y-spring (x load)



(c) u Displacement for x-spring (x load)



(d) v Displacement for x-spring (y load)

Fig. 15: Displacement results for x-spring and y-spring under x and y loads: (a) v Displacement for y-spring (y load), (b) u Displacement for y-spring (x load), (c) u Displacement for x-spring (x load), (d) v Displacement for x-spring (y load).

VI. CONCLUSIONS

The aim of this work is to verify the accuracy of the results reported in a study originally presented at the 2011 COMSOL Conference in Bangalore on a 3D accelerometer designed for automotive applications. The focus is on key parameters, including the equivalent elastic constant of the springs, maximum displacement, and maximum stress under horizontal and vertical loads. Additionally, for a fixed acceleration value (100 g), the dependence of the displacement on the angle between the x-axis and y-axis is analyzed.

The results obtained are consistent with the analytical calculations performed in the first section, although discrepancies are observed when compared to the results presented in the original study. Specifically, the equivalent elastic constants determined from the simulations align well with the analytical calculations conducted in this work. To enhance accuracy, additional simulations were performed for the individual springs (x-spring and y-spring), which also produced results consistent with those found in the initial simulations.

The evaluation of capacitance in the simulations is consistent with the analytical calculations, showing a very small variation depending on the load cases. This is in agreement with the small displacements observed in the simulations. However, the capacitance values found in this study differ from those reported in the original paper.

The most plausible explanation for these discrepancies lies in the incomplete specification of structural dimensions in the

original study, which makes precise comparisons challenging. By combining analytical studies with simulation results, this work provides a comprehensive analysis, offering insights into the mechanical and electrical behavior of the accelerometer under different loading conditions.

REFERENCES

- [1] S. Vijayakumar, G. Vijila, M. Alagappan, and A. Gupta, "Design and analysis of 3d capacitive accelerometer for automotive applications," *Unpublished Manuscript, PSG College of Technology*, 2011.
- [2] D. Xia, L. Kong, and H. Gao, "Design and analysis of a novel fully decoupled tri-axis linear vibratory gyroscope with matched modes," *Key Laboratory of Micro Inertial Instruments and Advanced Navigation Technology of the Ministry of Education, School of Instrument Science and Engineering, Southeast University*, Jul 2015.
- [3] G. Fedder, "Simulation of microelectromechanical systems," Ph.D. Thesis, University of California, Berkeley, Berkeley, CA, USA, 1994.